S1 Supplementary Material to Section "Data"

This supplementary section describes the data processing from raw GRACE/GRACE-FO satellite observations (level 0) to gridded terrestrial water storage (TWS) products (level 3) and the derivation of groundwater storage (GWS) anomalies in the Global Gravity-Based Groundwater Product (G3P, level 4). The GFZ and G3P data processing workflow follows a hierarchical approach, transforming raw satellite observations into global gravity field solutions and hydrological data products.

S1.1 Level 0 to Level 2: From Raw Observations to Gravity Field Solutions

Monthly snapshots of the Earth's gravity field are determined from GRACE and GRACE-FO satellite missions operating as free-fall experiments. The primary level 0 observations comprise kinematic satellite orbits determined by GPS (centimeter accuracy), inter-satellite distances measured by the K-band microwave link (micrometer accuracy) (Dunn et al., 2003), and accelerometer measurements capturing non-gravitational forces acting on the satellites (e.g., atmospheric drag, solar radiation pressure) (Tapley et al., 2004; Klinger and Mayer-Gürr, 2016). At Level 1, these data are pre-processed to derive satellite positions, inter-satellite distances, and accelerations.

The temporal and spatial resolution of gravity field solutions is limited by the cross-track separation of ground tracks, which depends on the orbital repeat cycle and Earth rotation (Weigelt et al., 2013). With approximately 15.3 revolutions per day, gravity fields up to degree and order 92 could theoretically be resolved every 6 days, but multiple sub-cycles must be accumulated to achieve adequate signal-to-noise ratios. Consequently, monthly gravity field solutions up to degree and order 96 have become the standard. Signal attenuation occurs due to orbit altitude (a trade-off between sensitivity and satellite lifetime), while noise comprises observation errors, background model uncertainties, and aliasing effects. Non-tidal mass variations of the ocean and atmosphere on sub-monthly time scales are reduced by the Atmosphere and Ocean De-aliasing Level-1B (AOD1B) product (Shihora et al., 2022). Strict uncertainty propagation is not feasible due to numerous poorly quantified error sources, requiring empirical calibration (Schmidt et al., 2007).

Independent level 2 gravity field solutions from multiple Analysis Centers are combined by the IAG Combination Service for Time-variable Gravity Fields (COST-G; Jäggi et al. 2020; Meyer et al. 2023) to reduce stochastic noise and provide consolidated monthly gravity field models distributed via ICGEM (`http://icgem.gfz-potsdam.de`) and GravIS (`http://gravis.gfz.de`).

S1.2 Level 2B: Spectral Domain Corrections

Before gridding, several corrections are applied in the spectral domain. A long-term mean gravity field (April 2002–December 2020) is subtracted, and Stokes coefficients are filtered using time-variable anisotropic VDK filters (VDK2, VDK3, VDK5; Horvath et al. 2018). These filters adapt month-by-month to account for temporal variations in error characteristics, providing optimal decorrelation and noise suppression for each individual monthly solution. Weakly observed coefficients are replaced: C_{20} for the entire GRACE/GRACE-FO period by Satellite Laser Ranging estimates (König et al., 2019); C_{30} during accelerometer degradation periods (November 2016–June 2017 for GRACE); and C_{21}/S_{21} for GFZ RL06 GRACE solutions (particularly the last 7 months). Degree 1 coefficients (geocenter motion) are approximated using Swenson et al. (2008). Long-term secular trends from Glacial Isostatic Adjustment are corrected using the ICE-6G_D (VM5a) model (Peltier et al., 2018), with coefficients of degrees 0 and 1 omitted from this correction. A 161-day harmonic signal (S2 tidal alias) is removed, with a

phase offset of 100° applied between GRACE and GRACE-FO to account for their non-aligned nodal planes.

S1.3 Level 3: Gridded Terrestrial Water Storage

Level 3 processing transforms the corrected spherical harmonic coefficients into global 0.5° grids of mass anomalies expressed as equivalent water height (Wahr et al., 1998). To reduce leakage effects while preserving signal quality, the data are decomposed into deterministic components (linear trend, annual, and semi-annual signals) and residual interannual signals. This strategic filtering approach takes deterministic signals from weakly filtered VDK5 fields and combines them with strongly filtered VDK3 residuals. The weaker VDK5 filtering for long-term trends and seasonal patterns minimizes signal attenuation for these well-determined components, while the stronger VDK3 filtering for residuals effectively suppresses high-frequency noise. For end-of-life GRACE months with insufficient VDK3 quality, VDK2 residuals are used. Co-seismic gravity field signals from the Sumatra–Andaman (2004), Chile (2010), and Japan (2011) earthquakes are removed. Ocean areas, Greenland, and Antarctica are masked (grid cells are classified as land if $\geq$50 % land coverage per ESA CCI 150 m mask).

Uncertainties are computed from the RMSE of residual signals over the open ocean (distance to coast >1000 km) scaled by a spatial covariance model (Boergens et al., 2020, 2022). These uncertainties are spatially constant for each time step but vary temporally depending on data quality. Final TWS products are distributed via GravIS (`https://gravis.gfz-potsdam.de`; Dahle et al. 2025).

S1.4 Level 4: Global Gravity-Based Groundwater Product (G3P)

GWS anomalies are derived from TWS using a water-balance approach where other continental water storage compartments are subtracted (Güntner et al., 2024; Güntner et al., 2026):

$$\mathrm{GWS} = \mathrm{TWS} - (\mathrm{RZSM} + \mathrm{SWE} + \mathrm{GM} + \mathrm{SWS}) \tag{S1}$$

The subtracted compartments are:

- **Root-zone soil moisture (RZSM):** To 2 m depth from Copernicus C3S surface soil moisture with gap filling and infiltration modeling (Pasik et al., 2023; Preimesberger et al., 2025). RZSM exhibits the largest uncertainties among all G3P components due to downward continuation from surface observations.
- **Snow water equivalent (SWE):** From GlobSnow (Luojus et al., 2021) combined with Copernicus CGLS operational SWE and global extension.
- **Glacier mass change (GM):** From C3S at monthly resolution (Dussaillant et al., 2023; Zemp and Welty, 2023).
- **Surface water storage (SWS):** Lakes, rivers, wetlands, reservoirs from OS LISFLOOD hydrological model simulations in GloFAS (Van Der Knijff et al., 2010; Choulga et al., 2024).

All monthly compartmental storage time series are spatially smoothed with a 250 km Gaussian filter to match the effective GRACE/GRACE-FO TWS resolution (approximately 300–500 km; Dahle et al. 2025; Sharifi et al. 2025). This spatial resolution harmonization is critical because GRACE-derived TWS exhibits spatially smoothed patterns due to orbit altitude and filtering, and uncompatible spatial structures between data sets would introduce spurious signals in the GWS residual. The filtered components are then subtracted from TWS to obtain GWS anomalies.

Uncertainties are propagated from individual components, representing measurement-system-type uncertainties (Merchant et al., 2017; Güntner et al., 2026). Uncertainties are further calibrated from the data to represent combined measurement noise and natural climate variability. All G3P storage data sets (V.1.12, nominal $0.5° \times 0.5°$ grid) are available via GravIS (Güntner et al., 2024).

S2 Supplementary Material to Section "Methods"

S2.1 Continental Mean Trends and Volume Budgets

This section describes the procedure used to derive continental water storage trends and volume balances from the G3P data. The methodology separates statistical summarization of spatial trends from physical volume integration, and ensures mass conservation and physically consistent continental and global aggregates.

The processing steps are as follows:

1. **Input data and significance filtering**
   Each grid cell is characterized by a linear trend estimate and its formal uncertainty (σ), derived from time series fitting, together with geographic coordinates. Only grid cells with statistically significant trends ($|b|/\sigma \geq 2.58$, two-sided 99% confidence level) are retained for further analysis, which limits the influence of noise-dominated regions.

2. **Geolocation and area calculation**
   Grid cells are assigned to continents using a shapefile of continental boundaries; cells falling outside polygons are assigned to the nearest region. Grid-cell surface areas are computed geodetically on the WGS84 ellipsoid based on the native grid spacing, which ensures area-aware aggregation.

3. **Physical volume integration**
   Continental volume change rates are computed by spatial integration of significant grid-cell trends:
   $$\Delta V = \sum_i A_i \cdot b_i \cdot 10^{-6},$$
   where b_i denotes the grid-cell trend ($\mathrm{mm\,yr^{-1}}$ equivalent water height) and A_i the corresponding grid-cell area ($\mathrm{km^2}$). The factor 10^{-6} converts $\mathrm{mm\,km^2}$ to $\mathrm{km^3}$, yielding volume change rates in $\mathrm{km^3\,yr^{-1}}$ (numerically equivalent to $\mathrm{Gt\,yr^{-1}}$ for freshwater). Positive and negative contributions are integrated separately to obtain gains, losses, and the net balance (ΔV). Because volume changes are obtained by direct summation of grid-cell contributions, they are physically additive.

4. **Global aggregation and validation**
   Global mean trends ($\mathrm{mm\,yr^{-1}}$) are computed as significant-area-weighted averages of continental trend estimates, while global volume changes are obtained by summing continental volume contributions. Mass-balance consistency is verified by ensuring that Gain – Loss $\approx \Delta V$.

S3 Supplementary Material to Section "Results"

S3.1 Supplementary Material to Section "Spectral Analysis"

Regarding the computation of GWS from TWS, we discuss the case for the global average PSDs of the observations (Figure S1, left panel) and the residuals (right panel). Ripples indicate the presence of spectral leakage from the trends that were reduced by the OLS regression. The

influence of trends is strongest for glaciers, as the PSD of the residuals drops significantly, consistent with its highest absolute trend magnitude shown in Figure 2 (main document). Most significant signals in the low-frequency band (below 1 cpy) contribute from trends in glacier mass. Clear contributions of trends are also obvious for SWS and TWS, followed by GWS, while trend contributions are more subtle for RZSM and SWE.

Regarding the inter-annual variations of the compartment variables, most power in the low-frequency band below 1 cpy is explained by RZSM, only dominated by glaciers at the very low periods (below 0.1 cpy). SWE and SWS contribute equally in magnitude at long to medium periods up to about 0.3 cpy, with magnitudes at the bottom end of the presented spectra. While the SWS (and also glaciers) drop, SWE variations keep a constant magnitude and reach a similar magnitude as RZSM signals at 1 cpy (while the latter still dominate until 1 cpy). Higher frequencies at intra-annual (above 1 cpy) are dominated by RZSM and SWE at similar magnitude, followed by SWS at quite constant magnitude, significantly below RZSM and SWE, but again approaching the PSD levels of RZSM and SWE for the frequencies near 6 cpy. While SWS and glaciers run quite similarly up to 1 cpy, higher-frequency contributions from glaciers become even more negative than SWS. For both the average PSD of the observations and residuals, it is notable that GWS clearly shows the reduction effects of the compartment variables across the whole frequency band, while it is, in terms of absolute power, still the dominant contributing variable to TWS, with only glaciers having a stronger contribution to TWS trend magnitude.

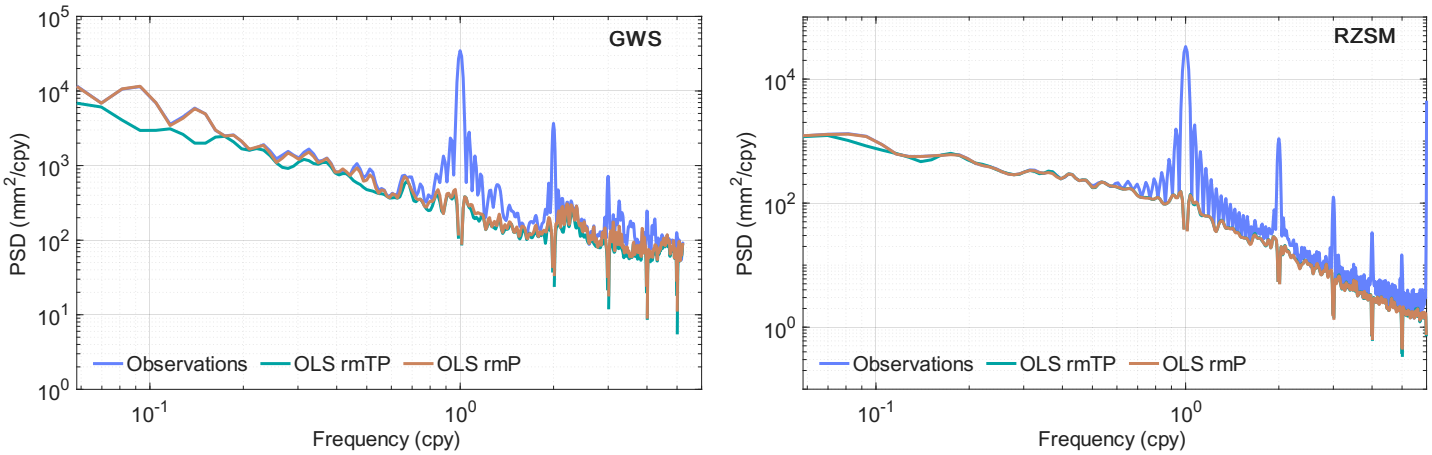

Figure S1: Globally averaged power spectral densities (PSDs) of groundwater storage (GWS, left) and root-zone soil moisture (RZSM, right), shown for the original time series, after removal of periodics (rmP), and after removal of both trends and periodics (rmTP).

To give more detailed insights into the effect of periodics and trends, we highlight important aspects from the globally averaged PSDs of GWS and RZSM (Figure S1, left and right-hand side). "rmP" stands for removal of periodics, "rmTP" stands for removal of trends and periodics. For RZSM, we clearly observe the periodics, and their removal has a strong effect on the spectral shape, which – besides a clear reduction of the peaks – also indicates disappearing spectral leakage. There is only a little reduction from trends, which indicates the primary contributions from inter-annual variations. This is different for GWS, as in the lower periods, the trend removal causes a clear drop in signal power. Effects of time-varying phase and amplitude can also be clearly studied from both GWS and RZSM, predominantly at the annual and semi-annual periods. Besides this, we can also observe the effects of cyclostationary seasonality, visible for GWS in the frequency band from 2 to 4 cpy.

S3.2 Supplementary Material to Section "Global Trends and Interpretation"

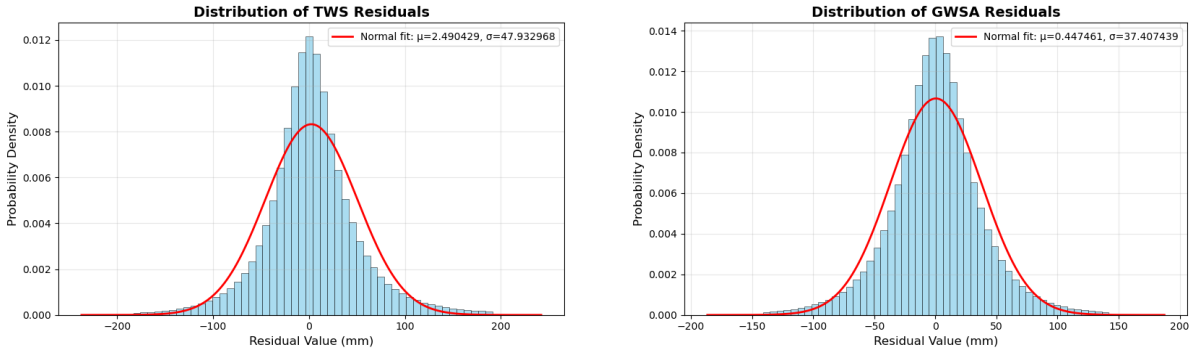

Figure S2: GRACE water storage residuals from all grid cells, shown as comprehensive distributions. To avoid distortion of the histogram scaling by a small number of extreme values, residuals beyond $\pm 3\sigma$ are omitted from the visualization only. Normal distributions are fitted to the displayed residuals, and both empirical histograms and fitted probability density functions are shown to assess approximate normality for TWS and GWS.

Normality diagnostics are computed for TWS and GWS (Figure S2), which constitute the primary targets of trend analysis in this study. This normality check underlines the reliability quality of trends and trend uncertainties estimated from these data, using the GLS estimator under serial autocorrelation.

Below, this supplementary section documents regional-scale details and interpretations, relating to the main text body. Figure 6 (main document) remains the main reference for significant TWS and GWS trends and is complemented by the storage-component trends in Figure 7 (main document).

Regarding North America: The strong TWS declines near the Gulf of Alaska (mass loss of approximately -60 km^3/yr during 2002–2016), caused by melting of glaciers such as the Malaspina, Columbia, and Bering glaciers. The Canadian Arctic Archipelago shows similarly strong negative trends from massive ice sheet loss (approximately -70 km^3/yr) (e.g., Wouters et al. 2019). The moderate TWS decay of about -5 to -10 mm/yr in the Northwest Territory of Canada (Mackenzie Basin, around Great Bear Lake) is not primarily linked to glacier melt but to long-term hydrological processes. Earlier GRACE analyses report declining TWS in the Mackenzie and Yukon basins, mainly due to permafrost thaw and groundwater discharge, combined with soil moisture changes, increased evapotranspiration, and the loss of surface water bodies linked to permafrost degradation (e.g., Lin et al. 2022; Wright et al. 2022). This pattern is consistent with persistently negative significant GWS trends at about the same magnitude, suggesting an ongoing descent of groundwater levels for these regions, driven by permafrost thaw and decreasing precipitation. The GWS pattern across the Alaska–Yukon region shows two negative zones separated by a positive corridor that extends from central Alaska into the Yukon region. The negative GWS trends (partly significant) along the Gulf of Alaska likely reflect residual leakage from intense glacier mass loss, rather than true groundwater depletion. Notably, the mild coastal negative anomaly in the north contrasts with earlier GRACE analyses (Muskett and Romanovsky, 2011), which reported slight GWS gains on the Arctic Coastal Plain for 2003–2009, possibly reflecting temporal changes in permafrost-hydrologic processes or methodological differences between products (aside limited data availability). While our 2002–2023 G3P analysis indicates localized positive trends in central zones extending from the Yukon region to central Alaska and southwestward toward the Yukon–Kuskokwim lowlands (at approximately $+5$ to $+10$ mm/yr), this is in contrast to earlier GRACE studies which report

groundwater losses across the Yukon River Basin through 2017 (Muskett and Romanovsky, 2011; Lin et al., 2022). Whether this discrepancy reflects temporal changes in hydrological regimes after 2017, methodological differences between G3P and earlier GRACE products, or limitations in signal separation in this glaciated and permafrost-dominated region remains unclear and requires further investigation. Across the western Canadian Arctic Archipelago, localized positive TWS and GWS trends are observed, contrasting with broader regional drying patterns. These trends occur in regions largely free of strong glacier loading, as major glacier mass loss is concentrated in the High Arctic (Queen Elizabeth Islands), away from Banks, Victoria, Melville, and Prince Patrick Islands (Noël et al., 2018; Gardner et al., 2011). While these islands are experiencing active permafrost degradation and thermokarst activity (Lewkowicz and Way, 2019; Rudy et al., 2017; Fraser et al., 2018) – processes that are typically associated with water mass loss – the mechanisms driving the observed positive storage trends remain unclear. Potential explanations include reduced rates of ice mass loss, residual GIA signal contamination, localized increases in precipitation or pooling surface water, or methodological artifacts in signal separation. In central and southwestern Canada (Alberta, Saskatchewan River Basin), we observe notable TWS declines that do not yet reach statistical significance, mostly due to high interannual variability. This becomes evident when analyzing the κ coefficient of the PL model, as seen from Figure S3, panel 1, which exhibits processes near random-walk behaviour. However, these patterns become more pronounced when examining GWS trends specifically, with significant declines evident in parts of the Saskatchewan River Basin. This is also supported by Figure S4, panel 1, which indicates that κ is much smaller, indicating that interannual variability has been reduced by the TWS-to-GWS reduction step. The negative GWS trends reflect sustained groundwater depletion from agricultural extraction (Hamdi and Goïta, 2023) combined with semi-arid climate conditions and recurring drought events, with TWS declining by more than 50 mm from 2002 levels due to severe drought conditions (Wang et al., 2025). The clearer GWS signal, relative to TWS, demonstrates the value of isolating anthropogenic extraction from natural climate variability using G3P GWS estimates. Similar patterns of TWS decline are observed in the Great Slave Lake region (central Northwest Territories), part of the Taiga Shield ecozone, where discontinuous permafrost degradation enhances groundwater connectivity and discharge (Wright et al., 2022). Regarding significance, GWS trends are more pronounced than TWS trends southwest of the lake, while both signals strengthen northeast toward Hudson Bay, reflecting spatial variability in permafrost conditions and hydrology. However, as discussed to the end of this results section, trends in RZSM and SWS variations also contribute notably to the negative budgets in these regions, with statistically significant trends peaking up to about -10 to -15 mm/yr. Note that this region experiences significant post-glacial isostatic adjustment, particularly near Hudson Bay, with model shortcomings that may still contribute to observed TWS/GWS spatial patterns. Earlier GRACE analyses showed slight positive TWS trends in eastern Canada, particularly east of Hudson Bay, attributed to precipitation variability (Li et al., 2016) (2003–2013). Our extended analysis, however, shows larger-scale drying for this area, with trends up to approximately -15 mm/yr. Similar negative trends are also reported in a recent analysis by Chandanpurkar et al. 2025, who document a transition from previously observed wetting to widespread drying across Northern Canada at -8.6 ± 0.3 mm/yr (excluding glaciers), driven primarily by permafrost melt. The intensified drying in Northern Quebec reflects accelerated permafrost degradation now exceeding -10 mm/yr, affecting GWS, and hence also TWS. In discontinuous permafrost regions, which dominate much of subarctic Canada, a 1-cm increase in active layer thickness corresponds to TWS decreases of more than 4 mm (Huang et al., 2025), explaining the strong negative trends and the pronounced shift from the wetting patterns reported by Li et al. (2016). This sensitivity is highest in discontinuous permafrost zones, where river discharge increases ($\sim$0.46 mm/yr) outpaces water inputs from precipitation minus evapotranspiration ($\sim$0.20 mm/yr), indicating net water mobilization from thawing subsurface reservoirs (Huang et al., 2025; Wang et al., 2025). In the Great Lakes Basin, water

levels transitioned from record lows in 2013 to record highs by 2017 (Gronewold and Rood, 2019), contributing to positive TWS trends in our 2002–2023 analysis. Our results indicate positive, though not statistically significant, GWS trends in the Great Lakes Basin. This is in contrast with earlier GRACE analyses, with limited data availability w.r.t. our study, covering 2002–2009 (Huang et al., 2012). The authors identified a GWS decline (5.2 ± 0.9 km^3/year) during the post-drought recovery period. The temporal difference likely reflects the post-2013 lake level recovery captured in our extended time series. Significant positive TWS and GWS trends are also observed across eastern Canada, extending from southern Quebec through the Ottawa Valley to the Ontario border, with particularly strong GWS signals in the region around Aiguebelle National Park. These positive trends reflect increased precipitation and enhanced groundwater recharge in cold and humid climate conditions (Dubois et al., 2022). However, our findings contrast with Fatolazadeh and Goïta (2021), who reported negative TWS trends along the Great Lakes northern edge and in coastal New Brunswick for 2002–2019, possibly reflecting differences in spatial resolution, time period coverage (their analysis ends in 2019 versus our 2023), or methodological approaches to GIA correction and signal processing. Regarding GWS in the eastern Canadian Arctic Archipelago (High Arctic, Queen Elizabeth Islands), we observe significant declines ranging from -5 to -20 mm/yr. These results should be interpreted cautiously, as they may be affected by imperfections in compartment variables (cf. main document Figure 7, panel a), signal leakage from Greenland, or errors in the GIA correction model. Generally, our observed groundwater declines in Canada are consistent with projected intensification of drought and soil moisture deficits in western North America under continued warming (Cook et al., 2020). Our investigation of G3P SWE trends (main document Figure 7, panel d) confirms strong negative trends in southwestern Canada and across the Canadian Pacific Northwest, which partly contribute (along with glacier retreat, panel a) to the negative TWS budget in this region. However, TWS trends in southwestern Canada do not yet reach statistical significance, indicating substantial contributions from inter-annual variability. Negative SWE trends are also evident in the eastern and northern drainage regions of Hudson Bay. In contrast, the Northwest (Yukon and Mackenzie basins) shows slightly positive SWE trends, making groundwater depletion the primary contributor to the observed negative TWS trends in these regions. A G3P SWS trend analysis (main document Figure 7, panel b) reveals negative anomalies around Williston Lake and Lake Winnipeg, slight negative trends around Great Slave and Great Bear Lakes, positive trends in the Great Lakes and southern Quebec, with neutral patterns elsewhere. These anomalies are generally consistent with documented regional processes: Williston Lake's negative signal may reflect substantial reduction in regulated Peace River peak flows due to dam operations (Beltaos and Peters, 2024), while Lake Winnipeg variability is affected by changing precipitation regimes and flooding dynamics in the Red River basin (Shrestha et al., 2012). Great Lakes positive trends correspond to observed high water levels during 2013–2020, with climate projections suggesting continued increases of approximately 0.2 to 0.4 m through mid-century (Kayastha et al., 2022). The spatial pattern of SWS changes shows general agreement with GRACE-based groundwater analyses indicating eastern Canada gains of approximately 5–10 mm/yr, contrasting with western losses (Li and Wang, 2022), suggesting that G3P SWS captures meaningful separation of surface water components from vertically-integrated TWS signals. G3P RZSM trends (main document Figure 7, panel b) show patterns consistent with observed TWS and GWS changes across Canada, supporting evidence of widespread drying, changing precipitation regimes, and permafrost thaw impacts in many regions. Altogether, negative SWS and RZSM trends underpin the ongoing drying across many regions in Canada, such as central and western Canada. These observations indicate that Canada is experiencing significant climate-driven changes in TWS. Further discussions of Canadian TWS and hydrological changes can be found in Rodell et al. (2018); Li et al. (2016); Bonsal et al. (2019); Li and Wang (2022).

Regarding South America: For Peru's coastal and Andean regions, satellite gravimetry

reveals a 30–40% decline in groundwater storage between 2003 and 2023, largely driven by anthropogenic extraction and climatic variability, as reported by (Gonzales et al., 2025).

Regarding Africa: While Boergens et al. 2024 noted strong interannual variability in East Africa without identifying long-term trends, and Li and Rodell 2024 observed sustained wetting in sub-Saharan Africa since 2019, attributed to climate drivers like La Niña and the positive IOD, our method's ability to distinguish long-term trends from short-term variability highlights that these positive anomalies may reflect significant long-term TWS changes.

Regarding Asia: In addition to the continent-scale summary in the main text, we note that discrepancies between well and satellite measurements in Middle and South India highlight the challenges of separating natural variability from anthropogenic activities within the resolution limits of GRACE/-FO (Dangar et al., 2021). We further note that signals in the Tazovsky district (West Siberia) are not extensively documented in the literature we reviewed; our findings there likely reflect permafrost-related hydrological changes and should continue to be monitored.

Regarding Oceania: The wet–dry spatial contrast across Australia is directly documented in the GRACE mascon trend maps and regional evaluations presented in Yang et al. (2020), which identify the Carpentaria Coast and North East Coast as areas of repeated water storage gains, and the North Western Plateau and western interior as regions with long-term deficits.

S3.3 Stochastic Model Parameters and Distributions

This section shows the stochastic model fit parameters for the power-law model κ parameter for the TWS (main document Figure 3) and GWS (main document Figure 4) time series data. Large negative values of κ (top panels) reflect strong correlations, and result in larger trend uncertainty (middle panels). For completeness, the bottom panels show the estimated trends (without significance indication). Figure S5 below shows the distributions of Figure S3 and S4. The median in the top panel indicate that estimated κ for both, TWS and GWS lie between flicker and random walk noise, with a correlation reduction from the TWS-to-GWS computation step (resulting from the removal of interannual signals). This also leads to reduced trend uncertainties (1 sigma) for GWS (Figure S5, middle panel) of about 2.6 mm/year in median. Panel c shows that GWS trends are smaller, which mostly results from the removal of ice mass trends by the TWS-to-GWS reduction step.

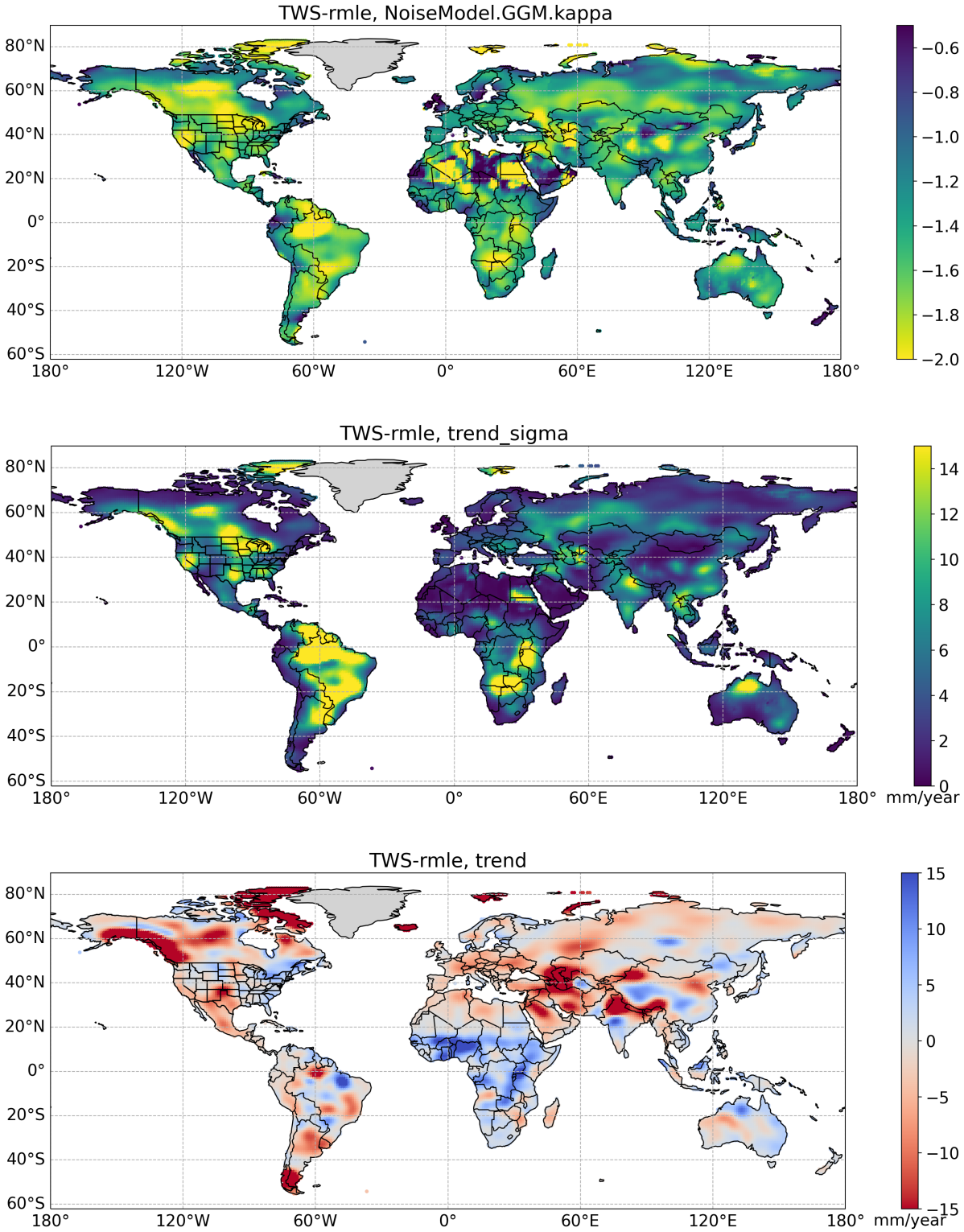

Figure S3: Estimated power law κ coefficient (top panel), trend uncertainties (1-sigma, middle panel) and trends (bottom panel) for TWS.

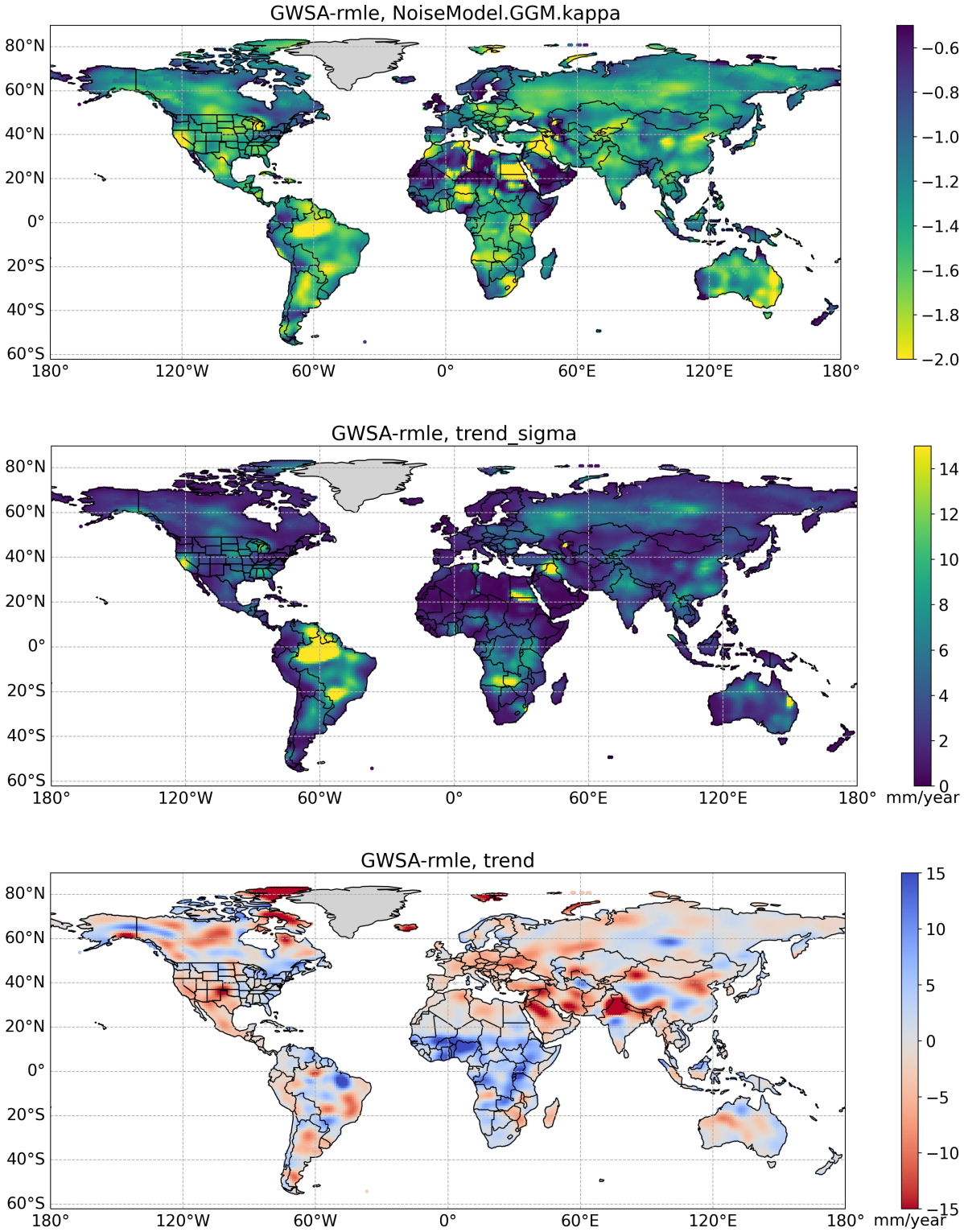

Figure S4: Estimated power law κ coefficient (top panel), trend uncertainties (1-sigma, middle panel) and trends (bottom panel) for GWS.

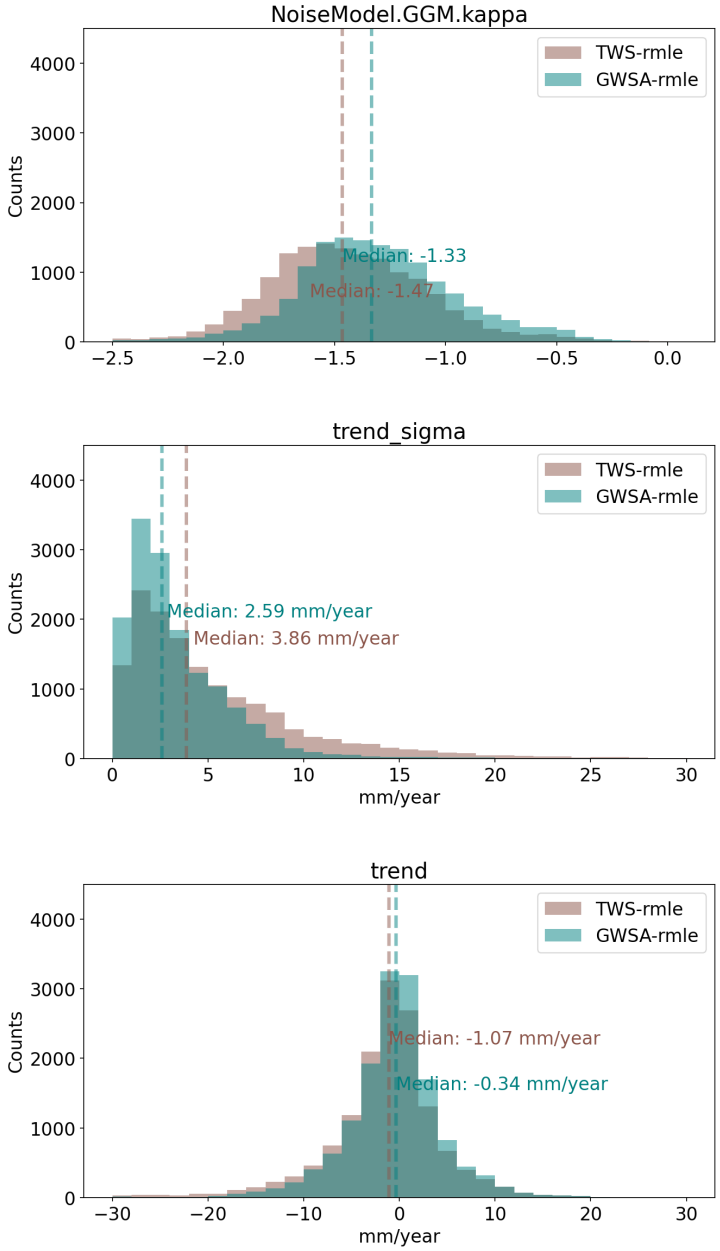

Figure S5: Histogram comparison of estimated power law κ coefficients (top panel), trend uncertainties (1-sigma, middle panel) and trends (bottom panel) for TWS and GWS, from Figure S3 and S4.

S3.4 95% Significance Trends

To assess the sensitivity of the detected GWS trends to the chosen significance threshold, Figure S6 shows the global distribution of significant TWS and GWS trends using a 95% confidence level (1.96 threshold). Overall, lowering the confidence threshold does not substantially alter the large-scale spatial patterns identified in the main analysis. As expected, areas of significant trends expand modestly, for example around Mexico City.

In Europe, the 95% threshold highlights more spatially continuous regions of significant drying, particularly in southern Germany and the Alpine region (Switzerland and Austria). More generally, a slightly larger fraction of grid cells approaches or exceeds significance in the Northern Hemisphere than in the Southern Hemisphere. This indicates that Northern Hemisphere groundwater signals are often closer to the detection threshold, consistent with

stronger long-term trends and/or lower relative noise levels, but does not change the overall interpretation of the results. Tables S1 and S2 report on the continentally aggregated trends and changes for the 95% confidence level.

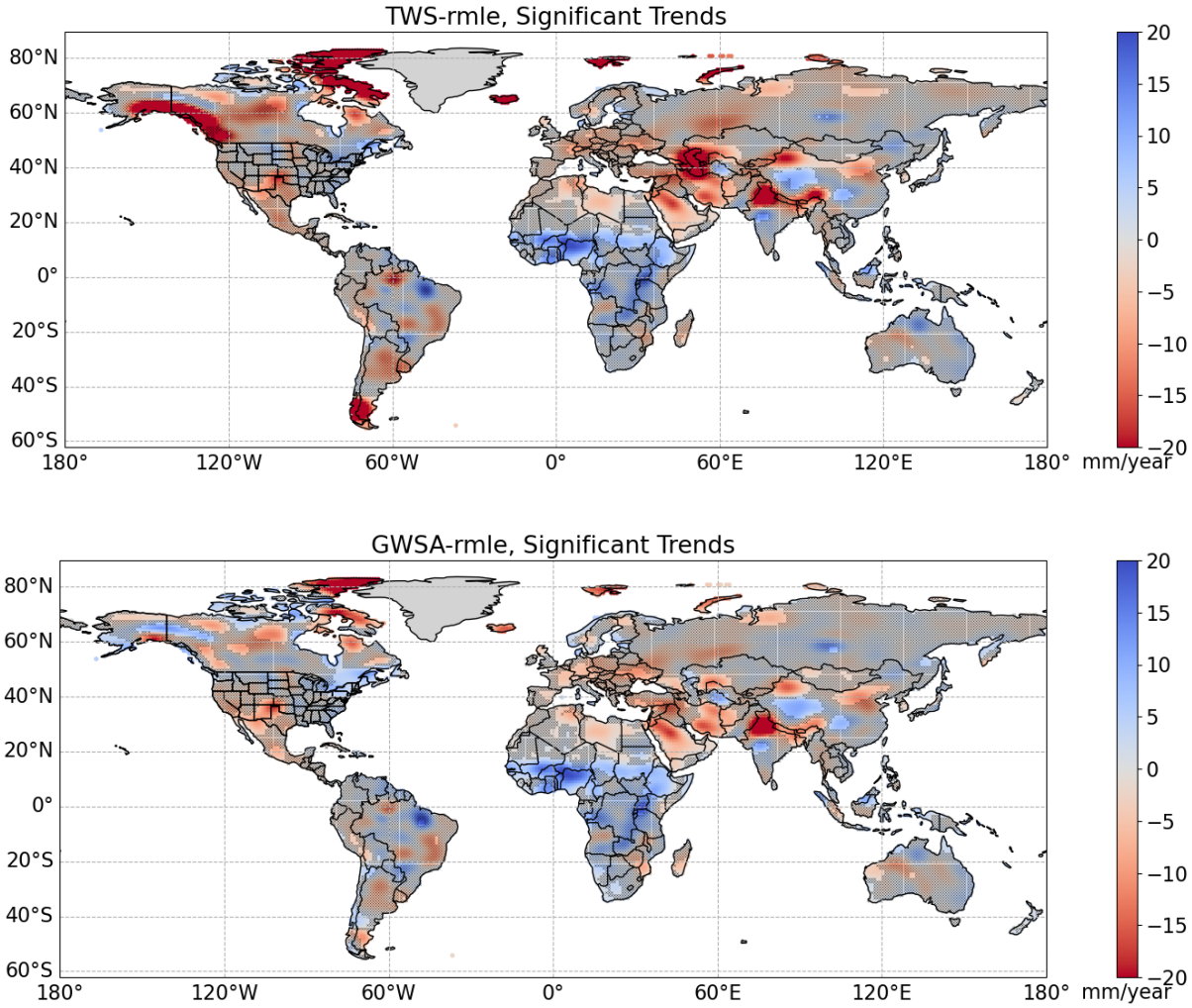

Figure S6: Significant TWS (top panel) and GWS trends (bottom panel) under consideration of 95% confidence interval. Shading with "X" represents data with insignificant trends, while all non-shaded trends represent statistically significant trends.

Table S1: TWS trend statistics by continent. Significant trends: $|\text{trend}|/\sigma \geq 1.96$ (95% confidence level). Mean trend: area-weighted mean. Volume totals: direct physical sum of $\sum A_i \cdot T_i \cdot 10^{-6}$. Global trend: significant-area-weighted mean.

Region	**Areal Coverage**			**Volume Change (km^3/yr)**			
	Area (10^6 km^2)	**Sig. Area** (10^6 km^2)	**Sig. Frac.**	**Trend** (mm/yr)	**Gain** (km^3/yr)	**Loss** (km^3/yr)	**V** (km^3/yr)
Africa	29.9	8.3	0.3	4.1	43.2	9.2	34.0
Asia	31.5	10.8	0.3	-9.0	13.0	110.0	-97.0
Europe	22.9	2.0	0.1	-10.4	1.4	21.8	-20.4
North America	21.2	4.2	0.2	-14.6	6.0	66.7	-60.7
Oceania	8.4	0.6	0.1	0.6	0.9	0.6	0.3
Seven seas (open ocean)	0.0	0.0	0.0	nan	0.0	0.0	0.0
South America	17.6	1.1	0.1	-16.0	0.3	17.6	-17.3
Global	**131.5**	**26.9**	**0.2**	**-6.0**	**64.8**	**225.9**	**-161.1**

Table S2: GWS trend statistics by continent. Significant trends: $|\text{trend}|/\sigma \geq 1.96$ (95% confidence level). Mean trend: area-weighted mean. Volume totals: direct physical sum of $\sum A_i \cdot T_i \cdot 10^{-6}$. Global trend: significant-area-weighted mean.

Region	**Areal Coverage**			**Volume Change (km^3/yr)**			
	Area (10^6 km^2)	**Sig. Area** (10^6 km^2)	**Sig. Frac.**	**Trend** (mm/yr)	**Gain** (km^3/yr)	**Loss** (km^3/yr)	**V** (km^3/yr)
Africa	29.9	11.3	0.4	4.1	56.9	10.7	46.2
Asia	31.5	10.8	0.3	-5.6	16.3	76.6	-60.2
Europe	22.9	3.0	0.1	-3.0	3.3	12.4	-9.0
North America	21.2	6.3	0.3	-1.4	16.3	24.9	-8.6
Oceania	8.4	1.0	0.1	0.2	1.5	1.2	0.2
Seven seas (open ocean)	0.0	0.0	0.0	nan	0.0	0.0	0.0
South America	17.6	1.2	0.1	-0.0	3.0	3.1	-0.0
Global	**131.5**	**33.6**	**0.3**	**-0.9**	**97.4**	**128.8**	**-31.4**

References

Beltaos, S., Peters, D.L., 2024. Effects of regulation on open-water flows in the lower Peace River, Canada, and implications for the recharge of Peace-Athabasca Delta basins. River Research and Applications 40, 151–162.

Boergens, E., Dobslaw, H., Dill, R., Thomas, M., Dahle, C., Murböck, M., Flechtner, F., 2020. Modelling spatial covariances for terrestrial water storage variations verified with synthetic GRACE-FO data. GEM-International Journal on Geomathematics 11, 24.

Boergens, E., Güntner, A., Sips, M., Schwatke, C., Dobslaw, H., 2024. Interannual variations of terrestrial water storage in the East African Rift region. EGUsphere 2024, 1–25.

Boergens, E., Kvas, A., Eicker, A., Dobslaw, H., Schawohl, L., Dahle, C., Murböck, M., Flechtner, F., 2022. Uncertainties of GRACE-Based Terrestrial Water Storage Anomalies for Arbitrary Averaging Regions. Journal of Geophysical Research: Solid Earth 127, e2021JB022081. doi:https://doi.org/10.1029/2021JB022081.

Bonsal, B.R., Peters, D.L., Seglenieks, F., Rivera, A., Berg, A., 2019. Changes in freshwater availability across Canada. Canada's changing climate report , 261–342.

Chandanpurkar, H.A., Famiglietti, J.S., Gopalan, K., Wiese, D.N., Wada, Y., Kakinuma, K., Reager, J.T., Zhang, F., 2025. Unprecedented continental drying, shrinking freshwater availability, and increasing land contributions to sea level rise. Science Advances 11, eadx0298.

Choulga, M., Moschini, F., Mazzetti, C., Grimaldi, S., Disperati, J., Beck, H., Salamon, P., Prudhomme, C., 2024. Technical note: Surface fields for global environmental modelling. Hydrology and Earth System Sciences 28, 2991–3036. doi:10.5194/hess-28-2991-2024.

Cook, B.I., Mankin, J.S., Marvel, K., Williams, A.P., Smerdon, J.E., Anchukaitis, K.J., 2020. Twenty-first century drought projections in the CMIP6 forcing scenarios. Earth's Future 8, e2019EF001461. doi:10.1029/2019EF001461.

Dahle, C., Boergens, E., Sasgen, I., Döhne, T., Reißland, S., Dobslaw, H., Klemann, V., Murböck, M., König, R., Dill, R., Sips, M., Sylla, U., Groh, A., Horwath, M., Flechtner, F., 2025. GravIS: Mass anomaly products from satellite gravimetry. Earth System Science Data 17, 611–631. doi:10.5194/essd-17-611-2025.

Dangar, S., Asoka, A., Mishra, V., 2021. Causes and implications of groundwater depletion in India: A review. Journal of Hydrology 596, 126103. doi:https://doi.org/10.1016/j.jhydrol.2021.126103.

Dubois, E., Larocque, M., Gagné, S., Braun, M., 2022. Climate change impacts on groundwater recharge in cold and humid climates: Controlling processes and thresholds. Climate 10, 6.

Dunn, C., Bertiger, W., Bar-Server, Y., Desai, S., Haines, B., Kuang, D., Franklin, G., Harris, I., Kruizinga, G., Meehan, T., Nandi, S., Nguyen, D., Rogstadd, T., Thomas, J.B., Tien, J., Romans, L., Watkins, M., Wu, S.C., Bettadpur, S., Kim, J., 2003. Instrument of GRACE. GPS World 14, 17–28.

Dussaillant, I., Bannwart, J., Paul, F., Zemp, M., 2023. Glacier mass change global gridded data from 1976 to present derived from the fluctuations of glaciers database. world glacier monitoring service. doi:10.24381/cds.ba597449.

Fatolazadeh, F., Goïta, K., 2021. Mapping terrestrial water storage changes in Canada using GRACE and GRACE-FO. Science of The Total Environment 779, 146435. doi:10.1016/j.scitotenv.2021.146435.

Fraser, R.H., Kokelj, S.V., Lantz, T.C., McFarlane-Winchester, M., Olthof, I., Lacelle, D., 2018. Climate sensitivity of high Arctic permafrost terrain demonstrated by widespread ice-wedge thermokarst on Banks Island. Remote Sensing 10, 954. doi:10.3390/rs10060954.

Gardner, A.S., Moholdt, G., Wouters, B., Wolken, G.J., Burgess, D.O., Sharp, M.J., Cogley, J.G., Braun, C., Labine, C., 2011. Sharply increased mass loss from glaciers and ice caps in the Canadian Arctic Archipelago. Nature 473, 357–360. doi:10.1038/nature10089.

Gonzales, L., López, V., Huamán, D., Villalobos, C., Espinoza, R., Vega, M., Ramos, J., 2025. Two decades of groundwater variability in Peru using satellite gravimetry data. Applied Sciences 15, 8071. doi:10.3390/app15148071. published 20 July 2025.

Gronewold, A.D., Rood, R.B., 2019. Recent water level changes across Earth's largest lake system and implications for future variability. Journal of Great Lakes Research 45, 1–3. doi:https://doi.org/10.1016/j.jglr.2018.10.012.

Güntner, A., Sharifi, E., Haas, J., Boergens, E., Cao, F., Dahle, C., Darbeheshti, N., Dobslaw, H., Dussaillant, I., Dorigo, W., et al., 2026. The global gravity-based groundwater product (G3P). Earth System Science Data Discussions 2026, 1–48.

Güntner, A., Sharifi, E., Haas, J., Boergens, E., Dahle, C., Dobslaw, H., Dorigo, W., Dussailant, I., Flechtner, F., Jäggi, A., Kosmale, M., Luojus, K., Mayer-Gürr, T., Meyer, U., Preimesberger, W., Ruz Vargas, C., Zemp, M., 2024. Global Gravity-based Groundwater Product (G3P) V.1.12. GFZ Data Services doi:10.5880/g3p.2024.001.

Hamdi, M., Goïta, K., 2023. Analysis of groundwater depletion in the saskatchewan river basin in Canada from coupled SWAT-MODFLOW and satellite gravimetry. Hydrology 10, 188.

Horvath, A., Murböck, M., Pail, R., Horwath, M., 2018. Decorrelation of GRACE time variable gravity field solutions using full covariance information. Geosciences 8, 323. doi:10.3390/geosciences8090323.

Huang, J., Halpenny, J., Van Der Wal, W., Klatt, C., James, T., Rivera, A., 2012. Detectability of groundwater storage change within the great lakes water basin using GRACE. Journal of Geophysical Research: Solid Earth 117.

Huang, Q., Wang, P., Wang, R., Yu, J., Frolova, N.L., Pozdniakov, S.P., 2025. Differential decline in terrestrial water storage across major permafrost-dominated Arctic River basins during the rapid warming period from 1981 to 2020. Journal of Geophysical Research: Atmospheres 130, e2024JD042978.

Jäggi, A., Meyer, U., Lasser, M., Jenny, B., Lopez, T., Flechtner, F., Dahle, Christophand Förste, C., Mayer-Gürr, T., Kvas, A., Lemoine, J.M., Bourgogne, S., Weigelt, M., Groh, A., 2020. International combination service for time-variable gravity fields (COST-G) - start of operational phase and future perspectives. International Association of Geodesy Symposia 152, 57–65. doi:10.1007/1345_2020_109.

Kayastha, M.B., Ye, X., Huang, C., Xue, P., 2022. Future rise of the Great Lakes water levels under climate change. Journal of Hydrology 612, 128205. doi:10.1016/j.jhydrol.2022.128205.

Klinger, B., Mayer-Gürr, T., 2016. The role of accelerometer data calibration within GRACE gravity field recovery: Results from ITSG-grace2016. Advances in Space Research 58, 1597–1609. doi:10.1016/j.asr.2016.08.007.

König, R., Schreiner, P., Dahle, C., 2019. Monthly Estimates of C(2,0) Generated by GFZ from SLR Satellites Based on GFZ GRACE/GRACE-FO RL06 Background Models. Technical Report. GFZ Data Services. doi:10.5880.

Lewkowicz, A.G., Way, R.G., 2019. Extremes of summer climate trigger thousands of thermokarst landslides in a high Arctic environment. Nature Communications 10, 1329. doi:10.1038/s41467-019-09314-7.

Li, B., Rodell, M., 2024. Terrestrial water storage in 2023. Nature Reviews Earth & Environment 5, 247–249.

Li, J., Wang, S., 2022. Seasonal variations and long-term trends of groundwater over the Canadian landmass. Hydrogeology Journal 30, 401–415. doi:10.1007/s10040-022-02460-1.

Li, J., Wang, S., Zhou, F., 2016. Time series analysis of long-term terrestrial water storage over Canada from GRACE satellites using principal component analysis. Canadian Journal of Remote Sensing 42, 161–170. doi:10.1080/07038992.2016.1166042.

Lin, H., Cheng, X., Zheng, L., Peng, X., Feng, W., Peng, F., 2022. Recent changes in groundwater and surface water in large pan-arctic river basins. Remote Sensing 14, 607.

Luojus, K., Pulliainen, J., Takala, M., Lemmetyinen, J., Mortimer, C., Derksen, C., Mudryk, L., Moisander, M., Hiltunen, M., Smolander, T., Ikonen, J., Cohen, J., Salminen, M., Norberg, J., Veijola, K., Venäläinen, P., 2021. GlobSnow v3.0 northern hemisphere snow water equivalent dataset. Scientific Data 8. doi:10.1038/s41597-021-00939-2.

Merchant, C.J., Paul, F., Popp, T., Ablain, M., Bontemps, S., Defourny, P., Hollmann, R., Lavergne, T., Laeng, A., De Leeuw, G., et al., 2017. Uncertainty information in climate data records from Earth observation. Earth System Science Data 9, 511–527.

Meyer, U., Lasser, M., Dahle, C., Förste, C., Behzadpour, S., Koch, Jäggi, A., 2023. Combined monthly GRACE-FO gravity fields for a global gravity-based groundwater product. Geophysical Journal International 236, 456–469. doi:10.1093/gji/ggad437.

Muskett, R.R., Romanovsky, V.E., 2011. Alaskan permafrost groundwater storage changes derived from GRACE and ground measurements. Remote Sensing 3, 378–397. doi:10.3390/rs3020378.

Noël, B., van de Berg, W.J., Machguth, H., Lhermitte, S., Howat, I., Fettweis, X., van den Broeke, M.R., 2018. Six decades of glacial mass loss in the Canadian Arctic Archipelago. Journal of Geophysical Research: Earth Surface 123, 1430–1449. doi:10.1029/2017JF004304.

Pasik, A., Gruber, A., Preimesberger, W., De Santis, D., Dorigo, W., 2023. Uncertainty estimation for a new exponential-filter-based long-term root-zone soil moisture dataset from Copernicus Climate Change Service (C3S) surface observations. Geoscientific Model Development 16, 4957–4976. doi:10.5194/gmd-16-4957-2023.

Peltier, R.W., Argus, D.F., Drummond, R., 2018. Comment on "An Assessment of the ICE-6G_C (VM5a) Glacial Isostatic Adjustment Model" by Purcell et al.: The ICE-6G_C (VM5a) GIA model. Journal of Geophysical Research: Solid Earth 123, 2019–2028. doi:10.1002/2016JB013844.

Preimesberger, W., Stradiotti, P., Dorigo, W., 2025. ESA CCI soil moisture gapfilled: an independent global gap-free satellite climate data record with uncertainty estimates. Earth System Science Data 17, 4305–4329.

Rodell, M., Famiglietti, J.S., Wiese, D.N., Reager, J., Beaudoing, H.K., Landerer, F.W., Lo, M.H., 2018. Emerging trends in global freshwater availability. Nature 557, 651–659.

Rudy, A.C.A., Lamoureux, S.F., Kokelj, S.V., Smith, I.R., England, J.H., 2017. Accelerating thermokarst transforms ice-cored terrain triggering a downstream cascade to the ocean. Geophysical Research Letters 44, 11,080–11,087. doi:10.1002/2017GL074912.

Schmidt, R., Flechtner, F., König, R., Meyer, U., Neumayer, K.H., Reigber, C., Rothacher, M., Petrovic, S., Zhu, S., Guenther, A., 2007. GRACE time-variable gravity accuracy assessment. International Association of Geodesy Symposia 130, 237–243. doi:10.1007/978-3-540-49350-1_36.

Sharifi, E., Haas, J., Boergens, E., Dobslaw, H., Güntner, A., 2025. GRACE-compatible filtering of water storage data sets via spatial autocorrelation analysis. Hydrology and Earth System Sciences 29, 6985–6998.

Shihora, L., Balidakis, K., Dill, R., Dahle, C., Ghobadi-Far, K., Bonin, J., Dobslaw, H., 2022. Non-tidal background modeling for satellite gravimetry based on operational ECWMF and ERA5 reanalysis data: AOD1B RL07. Journal of Geophysical Research: Solid Earth 127, e2022JB024360.

Shrestha, R.R., Dibike, Y.B., Prowse, T.D., 2012. Modelling of climate-induced hydrologic changes in the lake winnipeg watershed. Journal of Great Lakes Research 38, 83–94.

Swenson, S., Chambers, D., Wahr, J., 2008. Estimating geocenter variations from a combination of GRACE and ocean model output: ESTIMATING GEOCENTER VARIATIONS. Journal of Geophysical Research: Solid Earth 113. doi:10.1029/2007JB005338.

Tapley, B.D., Bettadpur, S., Ries, J.C., Thompson, P.F., Watkins, M.M., 2004. GRACE measurements of mass variability in the earth system. science 305, 503–505.

Van Der Knijff, J., Younis, J., De Roo, A., 2010. LISFLOOD: a GIS-based distributed model for river basin scale water balance and flood simulation. International Journal of Geographical Information Science 24, 189–212.

Wahr, J., Molenaar, M., Bryan, F., 1998. Time variability of the earth's gravity field: hydrological and oceanic effects and their possible detection using GRACE. Journal of Geophysical Research 103, 30205–30229. doi:10.1029/98JB02844.

Wang, S., Zhou, F., Fatolazadeh, F., Russell, H., Bunn, M., 2025. Accelerated water loss over Canada's landmass in 2002–2024 .

Weigelt, M., Sneeuw, N., Schrama, E., , Visser, P., 2013. An improved sampling rule for mapping geopotential functions of a planet from a near polar orbit. Journal of Geodesy 87, 127–142. doi:10.1007/s00190-012-0585-0.

Wouters, B., Gardner, A.S., Moholdt, G., 2019. Global glacier mass loss during the GRACE satellite mission (2002-2016). Frontiers in earth science 7, 96.

Wright, S.N., Thompson, L.M., Olefeldt, D., Connon, R.F., Carpino, O.A., Beel, C.R., Quinton, W.L., 2022. Thaw-induced impacts on land and water in discontinuous permafrost: A review of the Taiga Plains and Taiga Shield, northwestern Canada. Earth-Science Reviews 232, 104104.

Yang, X., Tian, S., Feng, W., Ran, J., You, W., Jiang, Z., Gong, X., 2020. Spatio-temporal evaluation of water storage trends from hydrological models over australia using GRACE mascon solutions. Remote Sensing 12, 3578.

Zemp, M., Welty, E., 2023. Temporal downscaling of glaciological mass balance using seasonal observations. Journal of Glaciology doi:10.1017/jog.2023.66.